1   **Lung infection by *P. aeruginosa* induces neuroinflammation and blood-brain barrier**

2   **dysfunction in mice**

3   Nuria Villalba[1], Yonggang Ma[1], Sarah A. Gahan, Aurelie Joly-Amado[1], Sam Spence, Xiaoyuan

4   Yang[1], Kevin Nash[1], Sarah Y. Yuan[1,2]

5   [1]Department of Molecular Pharmacology and Physiology, Morsani College of Medicine, University

6   of South Florida, Tampa, FL, USA. [2]Department of Surgery, Morsani College of Medicine,

7   University of South Florida, Tampa, FL, USA.

8

9

10

11

12

13   **Keywords:** Blood-brain barrier | Lung infection | Permeability

14

15

16

17   **Corresponding author:**

18   Sarah Y. Yuan, M.D., Ph.D.

19   Department of Molecular Pharmacology & Physiology

20   University of South Florida Morsani College of Medicine

21   Tampa, FL

22   syuan@usf.edu

23 **Abstract**

24 **Background**

25 Severe lung infection can lead to brain dysfunction and neurobehavioral disorders. The

26 mechanisms that regulate the lung-brain axis of inflammatory response to respiratory infection

27 are incompletely understood. This study examined the effects of lung infection causing systemic

28 and neuroinflammation as a potential mechanism contributing to blood-brain barrier (BBB)

29 leakage and behavioral impairment.

30 **Methods**

31 Pneumonia was induced in adult C57BL/6 mice by intratracheal inoculation of *Pseudomonas*

32 *aeruginosa* (PA). Solute extravasation, histology, immunofluorescence, RT-PCR, multiphoton

33 imaging and neurological testing were performed in this study.

34 **Results**

35 Lung infection caused alveolar-capillary barrier injury as indicated by leakage of plasma proteins

36 across pulmonary microvessels and histopathological characteristics of pulmonary edema

37 (alveolar wall thickening, microvessel congestion, and neutrophil infiltration). PA also caused

38 significant BBB dysfunction characterized by leakage of different sized molecules across cerebral

39 microvessels and a decreased expression of cell-cell junctions (VE-cadherin, claudin-5) in the

40 brain. BBB leakage peaked at 24 hours and lasted for 7 days post-inoculation. Additionally, mice

41 with lung infection displayed hyperlocomotion and anxiety-like behaviors. To test whether cerebral

42 dysfunction was caused by PA directly or indirectly, we measured bacterial load in multiple

43 organs. While PA loads were detected in the lungs up to 7 days post-inoculation, bacteria were

44 not detected in the brain as evidenced by negative cerebral spinal fluid (CSF) cultures and lack

45 of distribution in different brain regions or isolated cerebral microvessels. However, mice with PA

46 lung infection demonstrated increased mRNA expression in the brain of pro-inflammatory

47 cytokines (IL-1β, IL-6, and TNF-α), chemokines (CXCL-1, CXCL-2) and adhesion molecules

48 (VCAM-1 and ICAM-1) along with CD11b+ cell recruitment, corresponding to their increased

49 blood levels of white cells (polymorphonuclear cells) and cytokines. To confirm the direct effect of

50 cytokines on endothelial permeability, we measured cell-cell adhesive barrier resistance and

51 junction morphology in mouse brain microvascular endothelial cell monolayers, where

52 administration of IL-1β induced a significant reduction of barrier function coupled with tight junction

53 (TJ) diffusion and disorganization. Combined treatment with IL-1β and TNFα augmented the

54 barrier injury.

55 **Conclusions**

56 These results suggest that lung bacterial infection causes cerebral microvascular leakage and

57 neuroinflammation via a mechanism involving cytokine-induced BBB injury.

58

59

60

61

62

63

64

65

66

Introduction

Severe lung injury caused by bacterial infections may contribute to clinical complications such as multiple organ dysfunction, including cerebral and neurological disorders, which have been associated with high morbidity and mortality (1-3). Several factors, from pathogen load to duration of infection, determine patients' outcome with neuroinflammation as the link between long-term neurological damage and brain dysfunction resulting in a myriad of cognitive complications and behavioral symptoms.

The importance of lung-brain communication has been recognized based on strong clinical and experimental evidence. For example, clinical studies have demonstrated that patients with pneumonia often experience changes in mental status, such as confusion, low alertness and even delirium, specifically in older patients (4). Additionally, community-acquired pneumonia, the most prevalent cause of sepsis, can also induce acute and chronic changes in the central nervous system (CNS) (5-8). Sepsis-associated encephalopathy (SAE), a well-characterized state of long-term cognitive impairment and neurological dysfunction develops in approximately 70% of sepsis survivors (9). The causes of SAE are not completely understood albeit one of the explanations could be that a compromised BBB leads to brain dysfunction and CNS pathology (10, 11). A broad range of pathogens are capable of permanently or temporary affect brain functions (12, 13). Unlike viruses, which can infiltrate the CNS, direct dissemination of bacteria into the brain is rare and, therefore, other factors must contribute to the cerebral pathophysiology.

In the present study, we used a clinically relevant mouse model of bacterial pneumonia. We inoculated freshly prepared PA intratracheally into mice and examined the relationship between lung infection and cerebral dysfunction. Specifically, we tested whether the changes in the brain are due to a direct effect of bacteria penetrated the CNS, or indirectly via systemic and neuroinflammation triggered by pulmonary infection.

4

91 **Methods**

92 **Bacteria growth and inoculum preparation**

93 PA was selected for this study because it is known to be the most common cause of nosocomial

94 pneumonia (14). PA (PAO1 strain) (ATTCC; #27853) was cultured following manufacturer's

95 instructions. Prior to infection, freshly cultured bacteria from frozen aliquots (-80 °C) were grown

96 overnight at 37 °C in tryptic soy broth (Remel; #R455052) with vigorous agitation (180 rpm) and

97 harvested in log phase to an optical density at 600-nm (OD_{600}) of 0.3 (only for survival studies,

98 mice were inoculated with OD_{600} = 0.6). Bacteria were centrifuged at 3,000 rpm for 10 min, rinsed

99 and resuspended in sterile phosphate-buffered saline (PBS, pH 7.4). Serial dilutions and colony

100 count of the inoculum were performed to obtain the number of colony-forming units (CFUs) per

101 mL (CFU/mL). For histology experiments and multiphoton imaging, PA labelled with a green

102 fluorescent protein gene (PA-GFP; ATCC; #10145GFP) was used. PA-GFP was cultured in

103 nutrient agar (BD Difco^{TM}; #213000) or broth (BD Difco^{TM}; #234000) supplemented with 300 μg

104 ampicillin following manufacturer's instructions as described above and then inoculated into mice.

105 **Animal model of pneumonia**

106 Male and female C57BL/6 mice between 8 and 16 weeks of age were used in all experiments. All

107 mice were housed in a temperature and humidity-controlled housing with a 12-hour light:dark

108 diurnal cycle. Littermates of the same age were allocated to experimental groups. All experimental

109 animal protocols were approved by the University of South Florida Institutional Animal Care and

110 Use Committee (IACUC; protocol 8421R) and were conducted in accordance with the Guide for

111 Care and Use of Laboratory Animals.

112 Under anesthesia, forty-microliters of bacteria reconstituted in sterile PBS [OD_{600} = 0.3; 2×10^7

113 (CFUs/mL)] were directly injected into the mouse lungs by intratracheal instillation using a 22-G

114 cannula via the oropharynx using a mouse intubation kit (Hallowell EMC, MA) and an otoscope.

5

115　Control group received the same volume of sterile PBS (uninfected group). After inoculation, mice

116　were kept in a supine position for a few breaths or at least 30 seconds. Once awake, mice were

117　returned to their cages, monitored regularly and allowed access to food and water. For clinical

118　relevance, antibiotics (imipenem+cilastatin formulated in 0.9% saline solution) were administered

119　subcutaneously at a dose of 5 mg/Kg starting at 6 hours post-infection. The general conditions of

120　each mouse were monitored over a period of 7 days. All procedures were performed in a bio-

121　safety cabinet in a designated bio-safety level-II room according to the Biosafety protocols

122　approved by the University of South Florida.

123　**Measurement of microvascular permeability *in vivo***

124　The leakage of circulating solutes across microvessels was evaluated by measuring tissue (brain

125　and lung) accumulation of tracer molecules of different sizes using the ratiometric assay and near-

126　infrared imaging (NIR) as we previously described (15). Time-course of vascular permeability

127　changes was assessed in anesthetized mice intravenously injected through the retro-orbital

128　venous sinus with sodium fluorescein (NaFl; 5 µL/g of a 100 mg/mL NaFl solution; 376 Da; Sigma-

129　Aldrich; #6377) at 24 hours, 7 days and 1-month post-infection. Then, mice were anesthetized

130　with urethane (1.75 mg/Kg; intraperitoneally) and transcardially perfused with ice-cold 0.1 M PBS.

131　After dissection, brains and lung lobes were harvested, weighed and homogenized. Tissue

132　homogenates were centrifuged at 12,000 × g for 20 min at 4 °C. The fluorescence of a 100 µL

133　aliquot of the brain and lung samples along with 100 µL of blank or standards was measured on

134　a fluorescence microplate reader (SpectraMax M3; Molecular Devices, Sunnyvale, CA). The

135　concentrations of the samples were within the linear range of the standard curve. Amount of dye

136　(ng) was normalized per pg or µg protein in the extract.

137　In a different set of experiments, permeability to Alexa Fluor 70-kDa (5 µg/g of a 1 mg/mL solution;

138　Sigma-Aldrich; #R9379) was assessed in the lungs of controls and infected animals at 24 hours

139　post-infection. For NIR of lungs (left lobe), animals received albumin (Albumin-CF®680 dye; ⌒

140 70-kDa; 5 µg/g of a 1 mg/mL solution; Biotum; #20292). Tracer was allowed to distribute in freely

141 moving mice for 4 hours and then animals were cardially perfused with PBS. For NIR imaging of

142 brains, anesthetized animals received a combined injection of 10-kDa dextran (10 µg/g of a 1

143 mg/mL solution; CF^{TM}790-10-kDa dextran; #80121; Stellar Scientific) and albumin (Albumin-

144 CF®680 dye) intravenously. Organs (left lung lobe and whole brain) were imaged at 700 and

145 800 nm with a near-infrared imaging system (Odyssey CLx; LI-COR Biosciences, Lincoln, NE).

146 **Measurements of bacteria load in tissues and CSF**

147 Mouse lungs and spleen were harvested at different time points after infection, weighted and then

148 homogenized in tryptic soy broth under sterile conditions. One hundred µL of the homogenate

149 were plated on tryptic soy agar plates for quantification of colonies. CSF samples were obtained

150 under anesthesia through the cisterna magna using a custom-made glass cannula. Ten-fold serial

151 dilutions of the homogenates and CSF were prepared and spread onto agar plates. Next day,

152 CFUs were counted. For the identification of bacteremia (qualitatively), 100 µL of blood were

153 obtained under sterile conditions and cultured in culture vials (BD Bactec^{TM} peds plus culture

154 vials; #442020) for 4 days. Then, 100 µL of the culture vials were streaked onto a 5% sheep blood

155 in tryptic soy agar plates (Hardy diagnostics; #A10) for colony counts.

156 **Proinflammatory mediators in plasma and brain tissue**

157 Plasma samples obtained from blood collected by cardiac puncture in heparin tubes (BD

158 Microtainer® blood collection tubes; BD Biosciences; #365965) were analyzed for IL-6, IL-1β and

159 TNF-α using indirect sandwich enzyme-linked immunosorbent assay (ELISA) (Sigma-Aldrich;

160 #RAB0308 and #RAB0477) according to the manufacturer's instructions.

161 Total RNA was extracted from brain cortices and hippocampi from PA-infected and control

162 animals using TRIzol® Reagent (Invitrogen; #15596) and RNeasy Plus kit (Qiagen). RNA

163 concentration was measured using NanoDrop One Spectrophotometer (Thermo scientific).

7

164   Reverse transcription (RT)-PCR of RNA was performed using High-Capacity RNA-to-cDNA Kit

165   (Thermo Fisher Scientific; #4387406). cDNA was amplified for real-time detection with TaqMan^{TM}

166   Gene Expression Master Mix (Thermo Fisher Scientific; #4369016) plus individual primers for IL-

167   1β, IL-6, TNF-α, ICAM-1, VCAM-1, CXCL1 and CXCL2 (FAM tagged; Thermo Fisher Scientific)

168   on a Biorad CFX Connect^{TM} machine. Expression data were normalized to Gapdh mRNA levels.

169   The data were calculated as 2(Ct(Gapdh–gene of interest)) to compare infected group to controls.

170   MIQE guidelines were followed for all the PCR experiments and analysis (16).

171   **Flow Cytometry**

172   Mice were euthanized and perfused with sterile PBS through the left ventricle of the heart. The

173   brains (400-500 mg; without the cerebellum) were harvested, cut along the coronal plane with a

174   razor into three pieces and digested into cell suspensions using a Multi Tissue Dissociation kit 1

175   (Miltenyi Biotec, Germany; #130-110-201) and a gentleMACS^{TM} OctoDissociator with heaters

176   (Miltenyi Biotec; #130-096-427) following manufacturer's instructions. During the final steps,

177   myelin and erythrocytes were removed using a neural debris removal kit (Miltenyi Biotec; 130-

178   109-398) and red cell lysis solution (Biolegend; #420301), respectively. Total cell count in each

179   brain was quantified using a Luna-II automated cell counter. Cells were then subjected to antibody

180   staining for flow cytometry analysis. The cell suspension was stained with a panel of antibodies

181   against CD45-Alexa 700 (1:1200; Biolegend; #147716) and CD11b-PE dazzle (1:800; Biolegend;

182   #101256). A corresponding isotype IgG antibody was used as negative staining control. Dead

183   cells were excluded using the live/dead stain Zombie NIR fixable viability dye (1:2000; Biolegend;

184   #423105). The samples were run on a Cytek® Northern Lights^{TM} cytometer (Cytek biosciences)

185   and data were analyzed using FlowJo (FlowJo LLC, Ashland, OR). Cell populations were

186   calculated based on relative abundance obtained by flow cytometry (number = total cell count x

187   % of positive cells) (17). Cells were gated using FSCA and FSCH to identify singlets, then gated

188   for live cells by taking a population that was negative for live/dead stain. Antibodies concentrations

189 were chosen based on previous antibody titrations to determine the dilution that provides the best

190 separation of cell populations. Each "n" refers to a single brain obtained from a single mouse, so

191 that each n represents a different mouse. Brains were not pooled together for these experiments.

192 See Suppl. Fig. 1 for gating strategy used.

193 **Endothelial cell culture**

194 Primary mouse brain microvascular endothelial cells (Cell Biologics, Chicago, IL; #C57-6023)

195 were grown in the recommended culture medium (Cell Biologics; #M1168) supplemented with

196 10% (v/v) fetal calf serum at 37 °C and 5% CO_2, split at a ratio of 1:2 and used at passage two.

197 Endothelial cell monolayers were used for barrier integrity and immunofluorescence experiments.

198 **Assessment of barrier function by electric cell-substrate impedance sensing (ECIS) assay**

199 Barrier integrity of brain microvascular endothelial cells was performed using a protocol previously

200 described by our group (15, 18). Cell monolayers were grown to reach confluence in order to

201 obtain a polarized endothelium as evidenced by high and stable transendothelial electrical

202 resistance (TER, ohm) values (15). Mouse brain endothelial cell barrier function was determined

203 by measuring the cell-cell adhesion barrier resistance to electric current using an ECIS system

204 (Model ZƟ; Applied BioPhysics Inc., Troy, NY). Briefly, 250 μL of cell suspension (5 Å~ 105 cells

205 per mL) were seeded to each well of two ECIS culture arrays consisting of 8-wells with 10-gold

206 microelectrodes (8W1E+) following manufacturer's instructions. Resistance was recorded in real

207 time with the following settings: alternating current (1-volt) and 4-kHz frequency at 7-second

208 intervals. Data were normalized to baseline measurements just prior to the onset of treatment

209 (t=0) and expressed as resistance change (ohms). Both data acquisition and processing were

210 performed using the ECIS Z-theta Analysis Software supplied by Applied Biophysics to determine

211 the resistance (ohm @ 4kHz) values reflecting cell monolayer integrity and overall response to

212 cytokines. In a different set of experiments, cells were exposed to IL-1β (Miltenyi Biotec; #130-

213 094-053) and IL-1β + TNF-α (Biolegend; #575204). Cytokines were dissolved in PBS + 0.1% BSA

9

214 at 2, 20 and 200 ng/mL. Vehicle control was diluent alone at the same volume as treatment. Data

215 were normalized to baseline, and comparisons were made between cytokine treatment and

216 vehicle control. Data show mean ± S.E.M. (n=3).

Immunocytochemistry

218 Brain endothelial cell monolayers were plated on Lab-Tek® chamber slides (Thermofisher

219 Scientific; #1777399PK) and exposed to cytokines (IL-1β, 20 ng/mL), washed in PBS containing

220 2 mM $CaCl_2$ and 2 mM $MgCl_2$ and then fixed in 2% paraformaldehyde (PFA) in PBS for 5 min

221 followed by 4% PFA for 15 min. Cells were washed in PBS twice, permeabilized for 10 min (in

222 0.1% Triton-X/PBS) and blocked (10% normal donkey serum in 3% BSA/PBS) for 1 h at room

223 temperature. Slides were incubated with ZO-1 primary antibody (1:100; Thermofisher; #40-2200)

224 overnight at 4 °C. Next day, slide chambers were washed seven times and incubated with

225 appropriate secondary Alexa Fluor® antibodies (diluted at 1:500). Chambers were carefully

226 removed, and slides were then cover slipped using ProLong™ diamond antifade mountant with

227 DAPI (Life Technologies; #P36966).

Tissue processing and histology

229 Tissues (brain and lung) harvested from animals 24 hours after infection with GFP-labelled PA

230 were subjected to multiphoton imaging. Mice were anesthetized and injected intravenously with

231 200 µL of Evans blue solution containing 3% Evans blue fluorescent dye (Sigma-Aldrich; #E2129)

232 in 5% BSA/PBS to visualize vasculature prior to organ extraction and ex-vivo multiphoton imaging.

233 For visualizing PA distribution in tissue by confocal microscopy, mice infected with GFP-labelled

234 PA and controls were anesthetized and intracardially perfused through the left ventricle with PBS

235 and 4% PFA thereafter. Organs (lungs, spleen and brains) were post-fixed in 4% PFA overnight,

236 rinsed and preserved in 10% sucrose solution in PBS for one day or until the tissue sank to the

237 bottom. Mouse tissues were collected and embedded in Tissue Plus® O.C.T. compound (Fisher

10

238   HealthCare; #4585) in disposable base molds (Fisher HealthCare; #22363553). Blocks were then

239   frozen in liquid nitrogen and stored in –80 °C until sectioned in a cryostat. Frozen blocks were cut

240   into sections (15 μm thick) on a Leica CM1950 cryostat and slides were stored at –20 °C until

241   use. On the day of the experiment, slides were thawed in the hood overnight and stained with

242   Dylight 488-conjugated Lycopersicum esculentum lectin (1:100; Vector laboratories; #DL-1174)

243   to visualize brain microvessels. Slides were mounted in ProLongTM diamond antifade mountant

244   with DAPI.

245   Brain microvessels from control and PA-infected mice were freshly isolated from brain cortices as

246   previously described (19). Briefly, pial vessels were carefully removed, and the remaining tissue

247   was homogenized with a loose-fitting Dounce homogenizer in MCDB 131 medium. Homogenates

248   were then centrifuged for 5 min at 2,000g at 4 ºC. Pellets were resuspended in 15% (wt/vol)

249   dextran-PBS and centrifuged again at 10,000g for 15 min at 4 ºC. Myelin was carefully removed

250   from the tube and the pellet was removed with 1 mL DPBS and passed through a 40 μm strainer.

251   The strainer was reversed and washed with 10 mL MCDB 131 media to retrieve the microvessels.

252   Microvessels were fixed in 2% PFA and cytospinned onto microscope slides.

253   For immunohistochemistry, slides were permeabilized and blocked for 1 hour at RT in 10% normal

254   donkey serum diluted with PBS/3% BSA and 0.3 % Triton-X. Slides were incubated overnight with

255   the primary antibodies against neutrophils (1:100; Cederlane; #CL8993AP). Lectin was used to

256   label blood vessels. All antibody dilutions used were optimized by titration.

257   For visualizing lung structure, hematoxylin and eosin (H&E) staining was performed. Animals

258   were transcardially perfused via the left ventricle with PBS first and then 4% PFA. After one day

259   of post-fixation in the same fixative, lungs were embedded in paraffin using an automatic tissue

260   processor (Thermo Scientific) and then sectioned (4 μm) using a microtome. Slides were

261   deparaffinated and then stained with H&E following standard procedures. All slides were imaged

11

262   at the same time and using the same settings with a brightfield Olympus VS120 slide scanning

263   imaging system (x20 objective).

264   **Microscopy and Imaging**

265   Confocal microscopy was performed using two different lenses ×20 HC PL APO (0.75NA

266   [numerical aperture], WD [working distance] 0.62 mm) and a ×63 HC PL APO (Oil immersion,

267   1.4NA, WD 0.14 mm). Images were obtained as z-stacks using Leica STED SP8 Laser Confocal

268   Microscope and image software (LAS X). For confocal microscopy, GFP-labelled PA was excited

269   with the 488-nm laser.

270   Two-photon imaging was performed using an Olympus FV1000 MPE microscope equipped with

271   4 spectral detectors, a x25 XL Plan N 1.05 N.A. water immersion objective and a Coherent

272   Chameleon Ultra II IR laser. For multiphoton imaging, GFP-labelled PA was excited with 924-nm

273   laser pulses, emission was detected at 500–520 nm. Evans blue was excited at 945-nm and

274   detected at 620–750-nm. The raw 3D images were reconstructed from z-stacks using Imaris

275   software 9.7 (RRID:SCR_007370).

276   **Open field behavioral test**

277   Spontaneous locomotor activity and anxiety-like behavior were measured by open field test

278   assessed at 1-week after PA infection (20). Mice were placed in an open field chamber and were

279   allowed free exploration for 15 min. The distance traveled was recorded and analyzed using ANY-

280   maze® video tracking system (Stoelting Co, IL, USA). Increased overall distance travelled in the

281   chamber and time spent in the center were considered an index of greater locomotor activity and

282   anxiety-like behavior.

283   **Hematology and biochemistry**

284   White blood cell counts, cell differentials (neutrophils and monocytes) and total protein were

285   measured in mouse blood collected in heparin tubes using a ProCyte Dx hematology analyzer

286 (IDEXX, Westbrook, Maine). Blood pH was measured in fresh blood using an iSTAT device

287 (Abbott, Hightstown, New Jersey).

Statistical analysis

289 Data were analyzed using GraphPad Prism (version 9.4.0; GraphPad Software Inc., San Diego,

290 CA). Reported values are expressed as mean ± standard error of the mean (SEM). For animal

291 experiments, female and male mice were randomly selected and used as biological replicates.

292 Normality of the data was tested using the Shapiro–Wilk test. For data that were not normally

293 distributed (nonparametric data), the Mann–Whitney test (two groups, one variable) or Kruskal–

294 Wallis test followed by Dunn's correction (>2 variables) was used. Data with normal distribution

295 were analyzed   by a two-tailed unpaired Student's t–test (one variable) or one–way ANOVA with

296 Dunnett's or Tukey's correction (>2 variables). Statistical test used to analyze the data is

297 described in the figure legends. In all tests a 95% confidence interval was used. Figures show

298 exact P values.

Results

Effect of PA inoculation on mouse mortality and lung injury

301 PA-induced pneumonia was associated with mouse mortality, which depended on the inoculum's

302 load or number of infecting bacteria. Survival studies were performed using two inoculum's loads,

303 OD_{600} of 0.3 ($\sim2\times10^7$ CFUs/mL) and OD_{600} of 0.6. Infected mice with PA at an OD_{600} of 0.3 and

304 OD_{600} of 0.6 ($\sim9\times10^8$ CFUs/mL) induced a 16% and 50% mortality at day 7, respectively,

305 compared to 100% survival in the control group (Suppl. Fig 2a). All infected mice (OD_{600} 0.3)

306 showed lethargy, hypothermia and remained immobile or moved slowly in the cage starting at 4

307 hours post-infection (Suppl. Fig. 2b). Those who did not die within 24 hours showed significant

308 signs of improvement in mobility and appearance. Additionally, PA also caused acidosis and high

309 levels of proteins in the blood (hyperproteinemia), both metabolic parameters associated with

13

310   active infection (Suppl. Fig 2c,d). Together, these data support the validity of the PA-induced

311   pneumonia model.

312   Next, we assessed the pulmonary vascular barrier in vivo in PA infected mice (OD_{600} 0.3; 24 hours

313   post-infection) and uninfected controls by measuring extravasation of intravenously injected 70-

314   kDa fluorescent tracer. Upon PA challenge, plasma leakage from lung microvessels, indicated by

315   higher interstitial accumulation of 70-kDa dextran, was detected in infected mice compared with

316   that in controls (Fig. 1a,b). PA infection also caused a significant protein leakage (Fig. 1c). Lung

317   transvascular total protein flux increased by approximately 8-fold, peaked at 6 hours post-infection

318   and started to decrease by day 7 post-infection. H&E staining of lung sections post-infection

319   showed that PA evoked a robust inflammatory response (Fig. 1d). Compared to control lungs

320   characterized by thin alveolar walls and clear alveolar airspaces with few number of neutrophils

321   confined to the septal network, lung sections obtained from animals inoculated with PA were

322   characterized by congested vasculature, thickened alveolar walls with the presence of

323   microthrombi and alveolar infiltration of neutrophils (Fig. 1d,e).

BBB leakage following PA lung infection

325   Next, we studied whether PA-induced lung infection (OD_{600} 0.3) causes BBB permeability

326   changes. BBB leakage was first evaluated 24 hours after infection. We used NIR imaging of whole

327   brains after intravenous administration of 10-kDa and 70-kDa fluorescent tracers (Fig. 2a-d).

328   Significant leakage of both tracers into the brain parenchyma was detected in the infected group.

329   Importantly, paracellular permeability to 10-kDa dye was higher than the 70-kDa, suggesting a

330   size-depending opening of the BBB (Fig. 2a,d). The time-course of BBB permeability changes

331   ("BBB opening and recovery") was evaluated with NaFl at 24 hours, 7 days, and 1-month after

332   infection. Our results indicate a time-dependent increase in the degree of BBB hyperpermeability,

333   which peaked at 24 hours after lung infection and decreased by ~80% by 1-month post-infection

334   (Fig. 2e). The disruption of the BBB was associated with changes in mRNA expression of AJs

14

335 and TJs in the brain at different time points post-infection (Fig. 2f). VE-cadherin mRNA levels

336 decreased by day 7 and remained low 1-month after infection. Claudin-5 mRNA levels decreased

337 at earlier time points (24-hours) after infection while occludin mRNA levels remained unchanged.

Lung infection by PA causes anxiety-like behaviors

339 Next, we assessed both groups of mice for locomotor and anxiety-like behavior in an open field 7

340 days after saline or PA inoculation (OD_{600} 0.3) (Fig. 3a). PA infection increased the total distance

341 travelled in the open field (Fig. 3b) and decreased the amount of time animals remained immobile

342 (Fig. 3c); the amount of time spent in the brightly-lit center of the open field was higher in infected

343 animals compared to controls (Fig. 3d). The results of the open field test indicate PA-infected

344 animals had increased locomotor activity and anxiety-like behavior preferring to stay in the center

345 of the box compared with uninfected controls.

Tissue distribution of PA in vivo

347 We next characterized the spread of infection in mice intratracheally inoculated with PA (OD_{600}

348 0.3) 24 hours, 7 days, and 1-month after infection. We examined bacteria loads in the organs of

349 infected mice by quantifying CFUs in lung and spleen homogenates and CSF (Fig. 4a). In the

350 lungs, bacterial load decreased by ~4-fold 1-month after infection. PA load was also measured in

351 the spleen, which was used as a peripheral organ to assess whether there is systemic

352 dissemination of PA. In the spleen, PA was detected, although bacterial load was lower compared

353 to lung at all time points post-infection (Fig. 4a). Next, we evaluated the presence of PA in the

354 brain. We chose CSF for quantification of CFUs over homogenized brain tissue since ~90% of

355 infected animals showed bacteremia 24 hours post-inoculation and brains could be contaminated

356 with blood containing bacteria, which could provide misleading results. In parallel to the

357 quantification of bacterial loads, we performed confocal microscopy to visualize GFP-labeled PA

358 distribution within the lungs, spleen and brain. As shown in Figure 4b,c, 24 hours after infection

359 PA was detected with abundance in the lungs, mainly around the airways and spleen. In the brain,

360 we studied three putative sites of entry into the CNS: meningeal vessels, choroid plexus, brain

361 parenchyma, hippocampus and isolated brain microvessels (Fig. 4d-g). We did not detect PA in

362 any of those locations indicating the absence of PA infiltration into the CNS. Next, to confirm the

363 lack of distribution of PA in live tissue, we performed multi-photon microscopy in freshly harvested

364 lungs and brains 24 hours post-infection. The 3D reconstruction of z-stacks of brains and lungs

365 confirmed results seen on fixed tissues. In the lungs, PA was localized throughout the lung, while

366 no bacteria were detected in the brain parenchyma or inside brain capillaries (Suppl videos 1-4).

367 **Appearance of leukocytes in the CNS during PA pneumonia**

368 We next investigated the potential systemic effects of PA-induced lung infection. PA inoculation

369 (OD_{600} 0.3) into the lungs caused an increased level of total white blood cell count, along with

370 significantly higher number of neutrophils and monocytes 24 hours post-infection (Fig. 5a,b). In

371 addition, we studied whether PA pneumonia triggers an inflammatory response in the brain and

372 evaluated whether there is infiltration of circulating leukocytes into the brain and changes in

373 microglia number. In the CNS parenchyma, we found an abundant infiltration of leukocytes at 24

374 hours after infection. Subpopulations of leukocytes were discriminated according to the

375 expression of CD11b and CD45: microglia (CD11b$^+$ CD45^{low}), myeloid leukocytes (CD11b$^+$

376 CD45^{hi}) and non-myeloid leukocytes (CD11b$^-$ CD45^{hi}) (for gating strategy see Suppl. Fig. 1).

377 Analysis by flow cytometry confirmed elevated CD45$^+$ CD11b$^+$ cell numbers in the brain 24 hours

378 post-infection and no change in microglia retrieved from brain tissue (Fig. 5c,d).

379 **PA pneumonia upregulates systemic cytokines and causes neuroinflammation**

380 We next measured three representative systemic inflammation-derived proinflammatory

381 cytokines (IL-6, IL-1β and TNF-α) following PA administration (OD_{600} 0.3). There was significant

382 elevation of these proinflammatory cytokines in the plasma after lung infection peaking at early

383 time points (6-24 hours) (Fig. 6a,c). We also examined the brain's inflammatory state in vivo after

384 PA lung infection. Notably, our results showed an upregulated transcriptional expression of

385 cytokines (IL-1β, IL-6 and TNF-α), adhesion molecules (VCAM-1, ICAM-1) and chemokines

386 (CXCL1 and CXCL2) after infection in both brain cortex (Fig. 6d-f) and hippocampus (Fig. 6g-i).

Cytokine-induced brain endothelial barrier dysfunction

388 Cytokines are known to regulate not only immunity, but also barrier function (21-24). Once we

389 determined that PA lung infection increases the level of circulating cytokines and there is no direct

390 penetration of PA into the brain, we asked the question of whether circulating cytokines are

391 responsible for the disruption of the brain endothelial barrier leading to BBB leakage. Brain

392 microvascular endothelial cells were exposed for 24 hours to IL-1β (2, 20 and 200 ng/mL) and the

393 combination of IL-1β and TNF-α (20 ng/mL). We elected those cytokines because they were

394 highly expressed in the brain during PA pneumonia. Fig. 7a shows the impact of cytokine

395 exposure on barrier tightness. For IL-1β, TER was significantly decreased by 50% (Fig. 7a,b),

396 while the combination of cytokines caused a further decrease in TER (by 61%). In our previous

397 work, brain microvascular endothelial cells showed a tight monolayer within 5 days, expressing

398 ZO-1/claudin-5 and well-organized TJs, with a low permeability to small solutes (15). Next, we

399 studied the localization of the TJ protein ZO-1 upon IL-1ß treatment of brain endothelial cells (Fig.

400 7b). Endothelial cells under control conditions showed organized cell monolayers with clearly

401 visible ZO-1 immunostaining. At the TER maximum (approximately 2.5 hours after PA challenge),

402 TJ protein ZO-1 was still present outlining the outer of all cells under control conditions. After IL-

403 1ß treatment, ZO-1 immunostaining showed a diffused and discontinuous pattern with visible

404 intercellular gaps, where ZO-1 immunostaining was not fully outlining the circumference of each

405 cell, illustrating severe damage to the integrity of the endothelial cell layer.

Discussion

407 This study shows that PA pneumonia causes BBB leakage, neuroinflammation, and behavior

408 alteration (locomotor hyperactivity). The brain dysfunction occurred in the absence of direct

17

409   infection of the cerebral vasculature or brain parenchyma; thus, we propose that the underlying

410   mechanism involves an inflammatory response in the lung-brain axis linked by the circulation,

411   characterized by an increased expression of cytokines/chemokines and higher number of

412   leukocytes in the blood and CNS. This is further supported by our data showing that cytokines

413   exerted direct effects on cerebral microvascular endothelium to disrupt TJs, reduce cell-cell

414   adhesive barrier resistance, and increase BBB paracellular permeability.

415   PA is an opportunistic pathogen that can cause severe infectious disease in critically ill or

416   immunocompromised individuals (25). PA is responsible for a high percentage of hospital-

417   acquired pneumonia in patients on medical devices, such as ventilators or catheters, as well as

418   patients undergoing major surgeries (14, 26, 27). Compared to the lungs and other organs, brain

419   infection by PA is less common and limited to patients with head trauma or undergoing

420   neurosurgical procedures, such as intracranial catheterization where PA gains direct access to

421   the CNS (28, 29). In this study, we used a clinically relevant mouse model of pneumonia via

422   intratracheal delivery of PA. The animals received a moderate-to-high level of bacteria, which

423   resulted in ~50% mortality at 7 days post-infection. This is in agreement with a previous study

424   showing that administration of PA into murine lungs led to severe sepsis and death (30). In our

425   study, infected mice who survived for at least 24 hours demonstrated typical symptoms of acute

426   pneumonia, including low body temperature, high white blood cell and neutrophil counts, acidosis,

427   and proteinemia. Histopathological observations indicated that intratracheal inoculation of PA

428   triggered an inflammatory response in the lungs characterized by alveolar-capillary membrane

429   thickening and neutrophil infiltration. These changes coincided with pulmonary microvascular

430   thrombosis, damaged endothelial lining, and capillary leakage. Infected animals showed high

431   bacteria load in the lungs and blood stream. Together, these data support the validity of the PA-

432   induced pneumonia model.

433   Interestingly, while PA positive cultures were obtained in the spleen, an organ remote from the

434   lung, CSF cultures were negative. The absence of bacteria in the CNS is further supported by

435   immunofluorescence and multiphoton microscopic evidence confirming that in our murine model

436   of pneumonia, PA did not gain direct access to the brain. This finding is consistent with many

437   other studies showing that Pseudomonas meningitis is often post-neurosurgical, rather than

438   through direct penetration of PA into the CNS (26, 31, 32). On the other hand, lung infection

439   triggers a rapid and orchestrated activation of inflammatory cells and pathways leading to the

440   production of an array of inflammatory mediators. These mediators can target tissues remote from

441   the initial site of infection and cause multiple organ dysfunction. Within this context, the

442   pathophysiological importance of the inflammatory response in the lung-brain axis to bacterial

443   infection has been well recognized. For example, recent studies have identified lung amyloids,

444   tau proteins and endothelial glycocalyx fragments as bioproducts of acute lung infection can reach

445   the CNS and affecting learning and memory (33-36). However, the molecular mechanisms

446   underlying lung-brain interactions remain poorly understood. In particular, whether and how

447   bacteria invasion into the lung affects the BBB structure and function have not been well studied.

448   The present study provides novel evidence for the effects of PA lung infection on BBB

449   permeability.

450   The maintenance of brain homeostasis is largely controlled by the BBB, a specialized

451   neurovascular structure based on tightly sealed endothelial cells connected via cell-cell junctions

452   (e.g., occludin, claudin, cadherin) surrounded by pericytes and astrocytic end-feet (37). The BBB

453   exhibits a very low permeability and is highly restrictive to the passage of cells, solutes, and

454   pathogens, thus preventing neurotoxicity (38). During pathological states such as injury or

455   systemic inflammation, BBB breakdown leads to neuronal damage by allowing a plethora of

456   circulating agents to enter the brain. Our data suggest that the BBB function is compromised

457   during lung bacterial infection. In vivo, infected animals showed BBB leakage to tracers of different

458   sizes, especially small molecules (NaF and 10-kDa), which indicates an increased paracellular

459   permeability via compromised cell-cell junctions. Indeed, further molecular analyses showed a

460   decreased expression of claudin-5 (TJ) and VE-cadherin (AJ). We also observed a differential

461   response of these junction molecules at different times. For example, while claudin-5 levels

462   started to decline early (within 24 hours) post-infection, VE-cadherin decreased most significantly

463   during the late stage (days) after infection. In addition, the expression level of occludin remained

464   unaltered throughout the time course. There has been controversy regarding the role of occludin

465   in determining TJ strength and BBB permeability property; while one study showed that occludin

466   knockout mice present intact BBB (39), others have reported that changes in occludin expression

467   induced by proinflammatory cytokines lead to changes in paracellular permeability (40, 41).

468   As the endothelial barrier is in contact with circulating mediators whose levels vary under different

469   pathophysiological conditions (42), we sought to characterize the direct effects of proinflammatory

470   cytokines on BBB junction structure and function. Our model showed high levels of

471   proinflammatory cytokines in the plasma of infected animals, supporting that systemic

472   inflammation is part of disease progression following PA lung infection. In particular, the plasma

473   levels of TNF-α, IL-1β and IL-6 were significantly elevated. Importantly, we also detected an

474   increased expression of multiple cytokines and chemokines in the brain, with IL-1β and TNF-α as

475   the most significantly elevated in both cortex and hippocampus regions. Therefore, we selected

476   these cytokines for testing their effects on brain microvascular endothelial junctions in vitro. Our

477   barrier resistance (ECIS) data showed that IL-1β induced a dose-dependent reduction in TER,

478   indicator of cell-cell junction function, and this effect was augmented during combined treatment

479   with IL-1β and TNF-α. Structurally, compared to control brain endothelial monolayers showing

480   clearly defined TJs with continuous lining of ZO-1 at cell-cell contacts, IL-1β-treated endothelial

481   cells showed discontinuous junction lining with ZO-1 stained in a finger-like pattern and

482   intercellular gaps. These results reinforce the cytokines' ability to disrupt the BBB integrity.

483   Indeed, previous studies have demonstrated a correlation between in vivo administration of pro-

484   inflammatory cytokines and BBB leakage (39, 43). The ability of cytokines to open the paracellular

485   pathway of endothelial barrier has been attributed to endothelial cytoskeleton reorganization (24)

486   and/or downregulation of junction protein expression (22, 40, 44-50).

487   The microvascular leakage and BBB hyperpermeability observed in PA-infected animals were

488   associated with neuroinflammation, evidenced by immune cell recruitment and high expression

489   of proinflammatory cytokines, chemokines and adhesion molecules in the brain of mice with

490   pneumonia. It is known that lung infection or injury is associated with various neurological

491   complications, from altered memory to cognitive decline (51-54). In our model, even in the

492   absence of direct penetration of PA into the brain, infected mice developed anxiety-like behaviors,

493   which might result from cerebral microvascular dysfunction, BBB leakage, and systemic/local

494   production of cytotoxic cytokines like IL-1β (55-57) and TNF-α (47, 58) as previously documented.

495   **Conclusions**

496   The present study demonstrates that bacterial infection in the lungs causes neuroinflammation,

497   cerebral microvascular leakage and increased BBB paracellular permeability; the underlying

498   mechanisms involve cytokine-induced brain endothelial cell-cell adhesive barrier dysfunction and

499   TJ downregulation. These data provide novel evidence supporting the mechanistic linkage

500   between the lung and brain as part of an orchestrated host immune response to bacterial infection.

501   In addition, our study is unique because we have developed and validated a mouse model of

502   pneumonia that may prove useful in studying the brain sequelae of infectious diseases originated

503   from non-CNS organs.

504   **List of abbreviations**

505   AJs: Adherens junctions

506   BBB: Blood-brain barrier

507   CFUs: Colony forming units

508   CNS: Central Nervous System

509   ELISA: Enzyme-linked immunosorbent assay

510   GFP: Green fluorescent protein

511   H&E: Hematoxylin and Eosin

512   IL: Interleukin

513   NaFl: Sodium fluorescein

514   OD: Optical density

515   PA: Pseudomonas aeruginosa

516   PBS: Phosphate buffer saline

517   PFA: Paraformaldehyde

518   TER: Transendothelial electrical resistance

519   TJs: Tight junctions

520   TNF: Tumor necrosis factor

521   **Declarations**

522   **Competing interests**

523   The authors declare that they have no competing interests

524   **Funding**

527   **Author's contributions**

528   NV performed experiments, analyzed data and wrote the manuscript. YM and SS performed flow

529   cytometry experiments. SAG performed experiments, PA cultures and helped with data analysis.

530   AJA and KN helped with neurological testing experiments. XY helped with tissue/blood collection.

531   SYY conceptualize the study, edited and revised the manuscript and provided support through all

532   levels of development. All authors approved the final version of the manuscript.

533   **Acknowledgements**

534   No applicable

535   **Figure legends**

536   **Figure 1. Effects of PA pneumonia on lung inflammation.** (a) Representative NIR

537   fluorescence images of the left lung lobe obtained from control and PA infected mice (OD_{600} 0.3)

538   showing the distribution of 70-kDa tracer within the tissue. (b) Summary data showing lung

539   permeability of 70-kDa tracer. Mann-Whitney test, P=0.016 vs. control (uninfected) group. (c)

540   Plasma leakage indicated by increased levels albumin in bronchoalveolar lavage fluid (BALF).

541   Kruskal-Wallis test, P=0.0001, P=0.001 vs. control (uninfected) group. (d) Histological analysis

542   by conventional H&E staining of lung sections in control and PA infected mice (OD_{600} 0.3). (e)

543   Serial lung sections obtained from control and PA-infected mice immunostained for neutrophils

544   (red). Lectin (green) staining was used to visualized blood vessels and DAPI (blue) for nuclei. In

545   all graphs, each point indicates data from an individual animal, bar graphs (columns and error

546   bars) show mean ± S.E.M.

23

547 **Fig. 2. Effects of PA lung infection on BBB permeability and TJ expression.** Representative

548 NIR fluorescence images of whole brains obtained from control and PA infected mice (OD$_{600}$ 0.3)

549 showing the distribution of (a) 10-kDa and (c) 70-kDa tracers within the tissue. (b,d) Summary

550 data showing BBB paracellular permeability of 10-kDa and 10-kDa fluorescence tracers. Mann-

551 Whitney test, P<0.05 vs. control (uninfected) group. (e) Time course of BBB permeability changes

552 to small size solutes as measured by NaFl uptake starting at 24 h post-infection to 1-month post-

553 infection (OD$_{600}$ 0.3). Kruskal-Wallis test, P=0.01 and P=0.0002 vs. control (uninfected) group. (f)

554 Summary data showing mRNA expression levels of VE-cadherin, occludin and claudin-5 in brains

555 harvested from control and PA infected mice at 24 hours, 7 days and 1 month after infection.

556 Kruskal-Wallis test, P=0.01 and P=0.003 and P=0.002 vs. control (uninfected) group. In all graphs,

557 each point indicates data from an individual animal, bar graphs (columns and error bars) show

558 mean ± S.E.M.

559 **Fig. 3. Effect of PA pneumonia on mouse behavior.** (a) Representative tracks of control and

560 PA-infected mice (OD$_{600}$ 0.3) recorded by ANYMaze® video system during the open field test. (b)

561 Total distance traveled by control and PA-infected mice. (c) Time mice remained immobile in the

562 open field. (d) Time spent in the center of the open field by controls and PA-infected mice. Mann-

563 Whitney test, P=0.004, P=0.02, P=0.01 vs. control (uninfected) group. In all graphs, each point

564 indicates data from an individual animal, bar graphs (columns and error bars) show mean ± S.E.M.

565 In all graphs, each point indicates data from an individual animal, bar graphs (columns and error

566 bars) show mean ± S.E.M.

567 **Figure 4. PA load in peripheral organs and brain regions.** (a) Bacterial growth (CFUs per mg

568 of tissue) in lung, spleen and in brain (CSF) obtained from infected animals (OD$_{600}$ 0.3) and

569 controls after intratracheal administration of PA. (b) Representative confocal micrograph showing

570 (b) lung and (c) spleen sections obtained from GFP-labelled PA infected animals (OD$_{600}$ 0.3) and

571 controls. PA is labelled in green and nuclei (DAPI) in blue. (d-g) Representative confocal

572   micrographs of (d) cortical sections, (e) choroid plexus (f) hippocampus and (g) isolated capillaries

573   showing the lack of distribution of PA (GFP-labelled PA) in the brain of infected mice and controls.

574   Lectin (red) was used to label the blood vessels and DAPI (blue) for the nuclei.

575   **Fig. 5. Appearance of leukocytes in CNS during PA-induced lung infection.** (a) White blood

576   counts in control and PA-infected animals (OD_{600} 0.3). Mann-Whitney test, P=0.016 vs. control

577   (uninfected) group. (b) Neutrophil and monocyte counts in blood obtained from control and PA-

578   infected mice (OD_{600} 0.3) measured by ProCyte One hematology analyzer. Mann-Whitney test,

579   P=0.04, P=0.03 vs. control (uninfected) group. (c) Flow cytometry analysis of brain tissue

580   homogenates labeled with anti-CD45 and anti-CD11b antibodies with gating on CD45^{+} cells.

581   Quantitative analyses of (d) CD11b^{+} immune cell subpopulations and (e) microglia in control and

582   PA infected mice. Mann-Whitney test, P=0.03 vs. control (uninfected) group. In all graphs, each

583   point indicates data from an individual animal, bar graphs (columns and error bars) show

584   mean ± S.E.M.

585   **Fig. 6. PA lung infection causes systemic and neuroinflammation.** (a-c) PA-induced plasma

586   levels of IL-6, IL-1β and TNF-α at different time points after infection (OD_{600} 0.3) compared to

587   uninfected controls. Kruskal-Wallis test, P=0.01, P=0.001 and P=0.0009 vs. control (uninfected)

588   group. (d-f) mRNA expression levels of (d) cytokines (IL-1β, IL-6 and TNF-α), (e) chemokines

589   (CXCL1 and CXCL2) and (f) adhesion molecules (ICAM-1 and VCAM-1) in cortex from control

590   and infected mice. Mann-Whitney test, P=0.004, P=0.03, P=0.001, P=0.001 vs. control

591   (uninfected) group. (g-i) mRNA expression levels of (g) cytokines (IL-1β, IL-6 and TNF-α), (h)

592   chemokines (CXCL1 and CXCL2) and (i) adhesion molecules (ICAM-1 and VCAM-1) in

593   hippocampus from control and infected mice. Mann-Whitney test, P=0.01, P=0.005, P=0.01 vs.

594   control (uninfected) group. In all graphs, each point indicates data from an individual animal bar

595   graphs (columns and error bars) show mean ± S.E.M.

25

Fig. 7. Effect of proinflammatory cytokines on brain microvascular endothelial barrier function. (a) TER measurements across confluent monolayers of mouse brain microvascular endothelial cells incubated with IL-1β (2-200 ng/mL) and IL-1β+TNF-α (20 ng/mL each). The data were represented as resistance change. Mean $\pm$ S.E.M., n=3. Arrow indicates when cytokines were added. (b) Summary data showing drop in TER values (peak). (c) Immunocytochemical analysis of ZO-1 (green) on brain microvascular endothelial cells under control conditions (vehicle) or IL-1β treatment in vitro. Nuclei was stained with DAPI. White arrows indicate TJ disorganization.

Additional files.

Suppl. Fig. 1. (a) Representative flow cytometry plots illustrate the gating strategy used for this experimental series: single cell population (top left) was gated based on forward-scatter characteristics, Zombie viability dye was used to exclude dead cells (high fluorescence), and CD45 and CD11b staining were used to identify myeloid leukocytes (CD11b+ CD45^{hi}) and microglia (CD11b+ CD45^{low}) subpopulation of cells.

Suppl. Fig. 2. Effect of PA on mouse survival, body temperature and biochemistry parameters. (a) Survival rates of mice treated with PA at OD$_{600}$ 0.3 and 0.6. (b) Body temperature obtained by measuring the rectal temperature after PA infection (indicated by arrow). (c) Blood pH values obtained from control and PA-infected mice at 4 hours and 24 hours after infection measured with iSTAT. (d) Total protein (albumin and globulin) concentration in blood measured in controls and 24-hours after PA infection.

References

1.   McManus RM, Higgins SC, Mills KH, Lynch MA. Respiratory infection promotes T cell infiltration and amyloid-beta deposition in APP/PS1 mice. Neurobiol Aging. 2014;35(1):109-21.
2.   Rubin K, Glazer S. The pertussis hypothesis: Bordetella pertussis colonization in the pathogenesis of Alzheimer's disease. Immunobiology. 2017;222(2):228-40.

621   3.   Maheshwari P, Eslick GD. Bacterial infection and Alzheimer's disease: a meta-analysis. J
622   Alzheimers Dis. 2015;43(3):957-66.

623   4.   Janssens JP, Krause KH. Pneumonia in the very old. Lancet Infect Dis. 2004;4(2):112-24.

624   5.   Gofton TE, Young GB. Sepsis-associated encephalopathy. Nat Rev Neurol.
625   2012;8(10):557-66.

626   6.   Beutz MA, Abraham E. Community-acquired pneumonia and sepsis. Clin Chest Med.
627   2005;26(1):19-28.

628   7.   Ranzani OT, Prina E, Menendez R, Ceccato A, Cilloniz C, Mendez R, et al. New Sepsis
629   Definition (Sepsis-3) and Community-acquired Pneumonia Mortality. A Validation and Clinical
630   Decision-Making Study. Am J Respir Crit Care Med. 2017;196(10):1287-97.

631   8.   Rello J, Perez A. Precision medicine for the treatment of severe pneumonia in intensive
632   care. Expert Rev Respir Med. 2016;10(3):297-316.

633   9.   Ren C, Yao RQ, Zhang H, Feng YW, Yao YM. Sepsis-associated encephalopathy: a
634   vicious cycle of immunosuppression. J Neuroinflammation. 2020;17(1):14.

635   10.   Annane D, Sharshar T. Cognitive decline after sepsis. Lancet Respir Med. 2015;3(1):61-
636   9.

637   11.   Mazeraud A, Pascal Q, Verdonk F, Heming N, Chretien F, Sharshar T. Neuroanatomy
638   and Physiology of Brain Dysfunction in Sepsis. Clin Chest Med. 2016;37(2):333-45.

639   12.   Erkkinen MG, Berkowitz AL. A Clinical Approach to Diagnosing Encephalopathy. Am J
640   Med. 2019;132(10):1142-7.

641   13.   Dando SJ, Mackay-Sim A, Norton R, Currie BJ, St John JA, Ekberg JA, et al. Pathogens
642   penetrating the central nervous system: infection pathways and the cellular and molecular
643   mechanisms of invasion. Clin Microbiol Rev. 2014;27(4):691-726.

644   14.   Flanders SA, Collard HR, Saint S. Nosocomial pneumonia: state of the science. Am J
645   Infect Control. 2006;34(2):84-93.

646   15.   Villalba N, Baby S, Cha BJ, Yuan SY. Site-specific opening of the blood-brain barrier by
647   extracellular histones. J Neuroinflammation. 2020;17(1):281.

648   16.   Bustin SA, Benes V, Garson JA, Hellemans J, Huggett J, Kubista M, et al. The MIQE
649   guidelines: minimum information for publication of quantitative real-time PCR experiments. Clin
650   Chem. 2009;55(4):611-22.

651   17.   Ma Y, Yang X, Villalba N, Chatterjee V, Reynolds A, Spence S, et al. Circulating
652   lymphocyte trafficking to the bone marrow contributes to lymphopenia in myocardial infarction.
653   Am J Physiol Heart Circ Physiol. 2022;322(4):H622-H35.

18. Beard RS, Jr., Hoettels BA, Meegan JE, Wertz TS, Cha BJ, Yang X, et al. AKT2 maintains brain endothelial claudin-5 expression and selective activation of IR/AKT2/FOXO1-signaling reverses barrier dysfunction. J Cereb Blood Flow Metab. 2020;40(2):374-91.

19. Lee YK, Uchida H, Smith H, Ito A, Sanchez T. The isolation and molecular characterization of cerebral microvessels. Nat Protoc. 2019;14(11):3059-81.

20. Belzung C, Griebel G. Measuring normal and pathological anxiety-like behaviour in mice: a review. Behav Brain Res. 2001;125(1-2):141-9.

21. Capaldo CT, Nusrat A. Cytokine regulation of tight junctions. Biochim Biophys Acta. 2009;1788(4):864-71.

22. Rigor RR, Beard RS, Jr., Litovka OP, Yuan SY. Interleukin-1beta-induced barrier dysfunction is signaled through PKC-theta in human brain microvascular endothelium. Am J Physiol Cell Physiol. 2012;302(10):C1513-22.

23. Beard RS, Jr., Haines RJ, Wu KY, Reynolds JJ, Davis SM, Elliott JE, et al. Non-muscle Mlck is required for beta-catenin- and FoxO1-dependent downregulation of Cldn5 in IL-1beta-mediated barrier dysfunction in brain endothelial cells. J Cell Sci. 2014;127(Pt 8):1840-53.

24. de Vries HE, Blom-Roosemalen MC, van Oosten M, de Boer AG, van Berkel TJ, Breimer DD, et al. The influence of cytokines on the integrity of the blood-brain barrier in vitro. J Neuroimmunol. 1996;64(1):37-43.

25. Rello J, Rue M, Jubert P, Muses G, Sonora R, Valles J, et al. Survival in patients with nosocomial pneumonia: impact of the severity of illness and the etiologic agent. Crit Care Med. 1997;25(11):1862-7.

26. Rodriguez-Lucas C, Fernandez J, Martinez-Sela M, Alvarez-Vega M, Moran N, Garcia A, et al. Pseudomonas aeruginosa nosocomial meningitis in neurosurgical patients with intraventricular catheters: Therapeutic approach and review of the literature. Enferm Infecc Microbiol Clin (Engl Ed). 2020;38(2):54-8.

27. Huang CR, Lu CH, Chuang YC, Tsai NW, Chang CC, Chen SF, et al. Adult Pseudomonas aeruginosa meningitis: high incidence of underlying medical and/or postneurosurgical conditions and high mortality rate. Jpn J Infect Dis. 2007;60(6):397-9.

28. Chuang YC, Chang WN, Lu CH, Wu HS, Chang HW. Pseudomonas aeruginosa central nervous system infections: analysis of clinical features of 16 adult patients. Zhonghua Yi Xue Za Zhi (Taipei). 1999;62(5):300-7.

29. Boque MC, Bodi M, Rello J. Trauma, head injury, and neurosurgery infections. Semin Respir Infect. 2000;15(4):280-6.

687   30.   Bragonzi A. Murine models of acute and chronic lung infection with cystic fibrosis
688   pathogens. Int J Med Microbiol. 2010;300(8):584-93.

689   31.   Gallaher C, Norman J, Singh A, Sanderson F. Community-acquired Pseudomonas
690   aeruginosa meningitis. BMJ Case Rep. 2017;2017.

691   32.   Batlle Almodovar Mdel C, Dickinson F, Perez Monras M, Tamargo Martinez I, Similis A.
692   [Bacterial meningitis and Pseudomonas aeruginosa: apropos of a case]. Rev Cubana Med Trop.
693   2005;57(3):230-2.

694   33.   Balczon R, Lin MT, Lee JY, Abbasi A, Renema P, Voth SB, et al. Pneumonia initiates a
695   tauopathy. FASEB J. 2021;35(9):e21807.

696   34.   Scott AM, Jager AC, Gwin M, Voth S, Balczon R, Stevens T, et al. Pneumonia-induced
697   endothelial amyloids reduce dendritic spine density in brain neurons. Sci Rep. 2020;10(1):9327.

698   35.   Balczon R, Pittet JF, Wagener BM, Moser SA, Voth S, Vorhees CV, et al. Infection-induced
699   endothelial amyloids impair memory. FASEB J. 2019;33(9):10300-14.

700   36.   Hippensteel JA, Anderson BJ, Orfila JE, McMurtry SA, Dietz RM, Su G, et al. Circulating
701   heparan sulfate fragments mediate septic cognitive dysfunction. J Clin Invest. 2019;129(4):1779-
702   84.

703   37.   Sweeney MD, Zhao Z, Montagne A, Nelson AR, Zlokovic BV. Blood-Brain Barrier: From
704   Physiology to Disease and Back. Physiol Rev. 2019;99(1):21-78.

705   38.   Pardridge WM. Drug transport across the blood-brain barrier. J Cereb Blood Flow Metab.
706   2012;32(11):1959-72.

707   39.   Saitou M, Furuse M, Sasaki H, Schulzke JD, Fromm M, Takano H, et al. Complex
708   phenotype of mice lacking occludin, a component of tight junction strands. Mol Biol Cell.
709   2000;11(12):4131-42.

710   40.   Rochfort KD, Collins LE, Murphy RP, Cummins PM. Downregulation of blood-brain barrier
711   phenotype by proinflammatory cytokines involves NADPH oxidase-dependent ROS generation:
712   consequences for interendothelial adherens and tight junctions. PLoS One. 2014;9(7):e101815.

713   41.   Van Itallie CM, Fanning AS, Holmes J, Anderson JM. Occludin is required for cytokine-
714   induced regulation of tight junction barriers. J Cell Sci. 2010;123(Pt 16):2844-52.

715   42.   Tunkel AR, Rosser SW, Hansen EJ, Scheld WM. Blood-brain barrier alterations in
716   bacterial meningitis: development of an in vitro model and observations on the effects of
717   lipopolysaccharide. In Vitro Cell Dev Biol. 1991;27A(2):113-20.

718   43.   Saija A, Princi P, Lanza M, Scalese M, Aramnejad E, De Sarro A. Systemic cytokine
719   administration can affect blood-brain barrier permeability in the rat. Life Sci. 1995;56(10):775-84.

720   44.   Rochfort KD, Collins LE, McLoughlin A, Cummins PM. Tumour necrosis factor-alpha-
721   mediated disruption of cerebrovascular endothelial barrier integrity in vitro involves the production
722   of proinflammatory interleukin-6. J Neurochem. 2016;136(3):564-72.

723   45.   Rochfort KD, Cummins PM. Cytokine-mediated dysregulation of zonula occludens-1
724   properties in human brain microvascular endothelium. Microvasc Res. 2015;100:48-53.

725   46.   Rochfort KD, Cummins PM. The blood-brain barrier endothelium: a target for pro-
726   inflammatory cytokines. Biochem Soc Trans. 2015;43(4):702-6.

727   47.   Versele R, Sevin E, Gosselet F, Fenart L, Candela P. TNF-alpha and IL-1beta Modulate
728   Blood-Brain Barrier Permeability and Decrease Amyloid-beta Peptide Efflux in a Human Blood-
729   Brain Barrier Model. Int J Mol Sci. 2022;23(18).

730   48.   Pediaditakis I, Kodella KR, Manatakis DV, Le CY, Barthakur S, Sorets A, et al. A
731   microengineered Brain-Chip to model neuroinflammation in humans. iScience.
732   2022;25(8):104813.

733   49.   Haines RJ, Beard RS, Jr., Wu MH. Protein tyrosine kinase 6 mediates TNFalpha-induced
734   endothelial barrier dysfunction. Biochem Biophys Res Commun. 2015;456(1):190-6.

735   50.   Haines RJ, Beard RS, Jr., Chen L, Eitnier RA, Wu MH. Interleukin-1beta Mediates beta-
736   Catenin-Driven Downregulation of Claudin-3 and Barrier Dysfunction in Caco2 Cells. Dig Dis Sci.
737   2016;61(8):2252-61.

738   51.   Quilez ME, Fuster G, Villar J, Flores C, Marti-Sistac O, Blanch L, et al. Injurious
739   mechanical ventilation affects neuronal activation in ventilated rats. Crit Care. 2011;15(3):R124.

740   52.   Gonzalez-Lopez A, Lopez-Alonso I, Aguirre A, Amado-Rodriguez L, Batalla-Solis E,
741   Astudillo A, et al. Mechanical ventilation triggers hippocampal apoptosis by vagal and
742   dopaminergic pathways. Am J Respir Crit Care Med. 2013;188(6):693-702.

743   53.   Pelosi P, Ferguson ND, Frutos-Vivar F, Anzueto A, Putensen C, Raymondos K, et al.
744   Management and outcome of mechanically ventilated neurologic patients. Crit Care Med.
745   2011;39(6):1482-92.

746   54.   Huang HY, Huang CY, Li LF. Prolonged Mechanical Ventilation: Outcomes and
747   Management. J Clin Med. 2022;11(9).

748   55.   Michael BD, Griffiths MJ, Granerod J, Brown D, Keir G, Wnek M, et al. The Interleukin-1
749   Balance During Encephalitis Is Associated With Clinical Severity, Blood-Brain Barrier
750   Permeability, Neuroimaging Changes, and Disease Outcome. J Infect Dis. 2016;213(10):1651-
751   60.

752   56.   Labus J, Hackel S, Lucka L, Danker K. Interleukin-1beta induces an inflammatory
753   response and the breakdown of the endothelial cell layer in an improved human THBMEC-based
754   in vitro blood-brain barrier model. J Neurosci Methods. 2014;228:35-45.
755   57.   Melnikov PA, Valikhov MP, Kuznetsov, II, Grinenko NF, Sukhinich KK, Simbirtsev AS, et
756   al. Analysis of the Effect of IL-1beta on Blood-Brain Barrier Permeability in M6 Glioma Mouse
757   Model Using Intravital Microscopy. Bull Exp Biol Med. 2019;168(1):118-24.
758   58.   Nishioku T, Matsumoto J, Dohgu S, Sumi N, Miyao K, Takata F, et al. Tumor necrosis
759   factor-alpha mediates the blood-brain barrier dysfunction induced by activated microglia in mouse
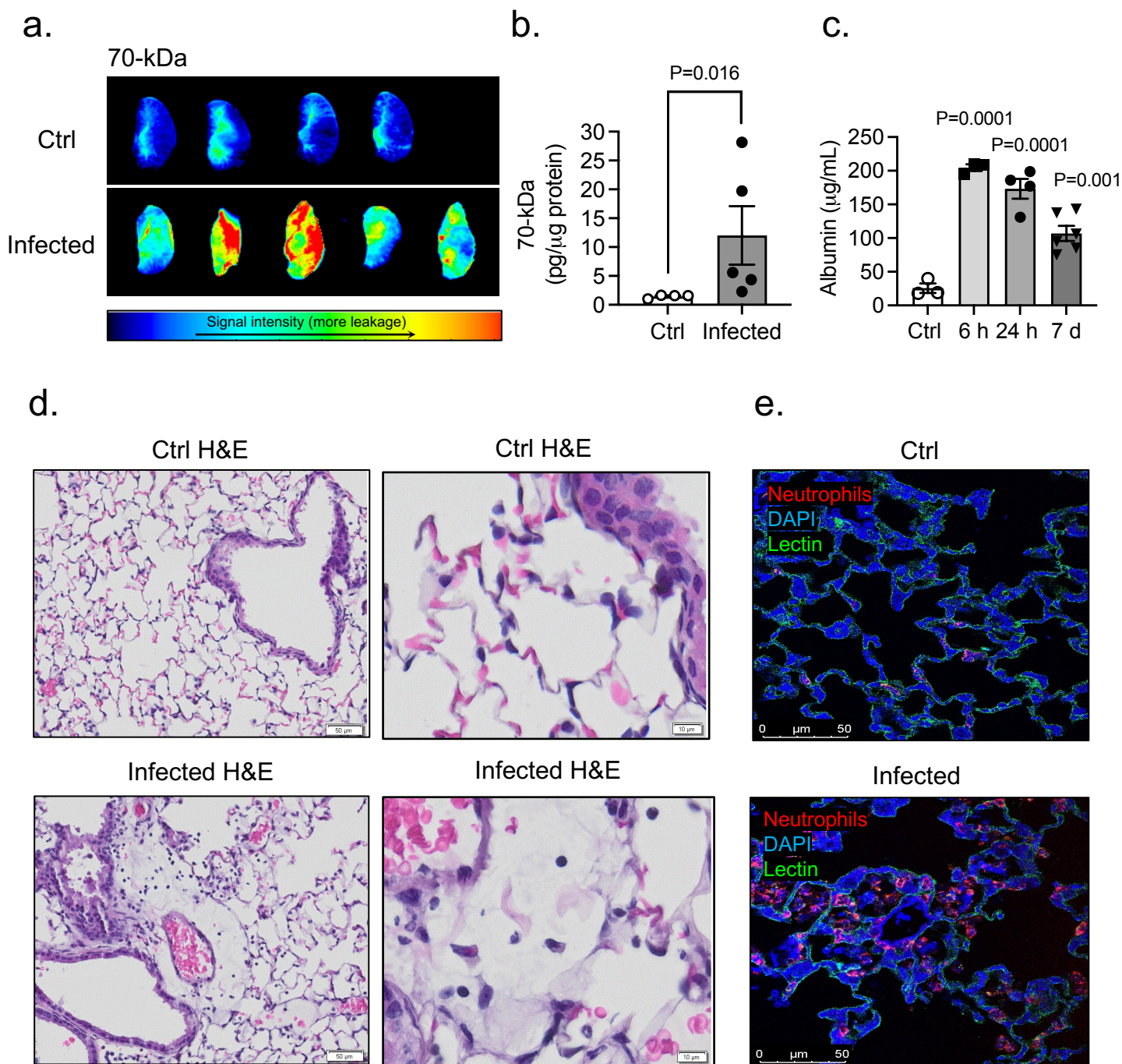760   brain microvascular endothelial cells. J Pharmacol Sci. 2010;112(2):251-4.
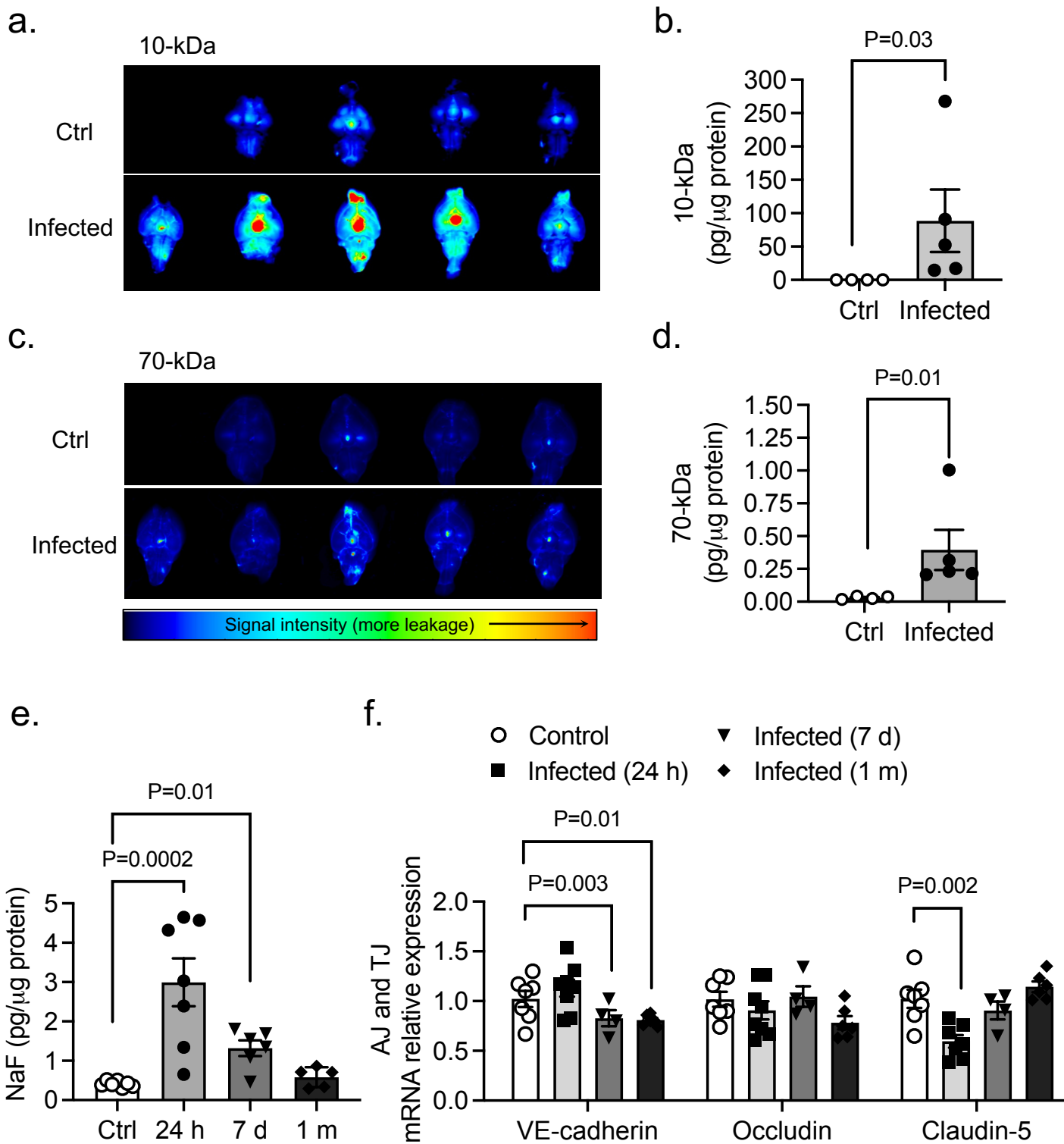
761

Fig. 1.

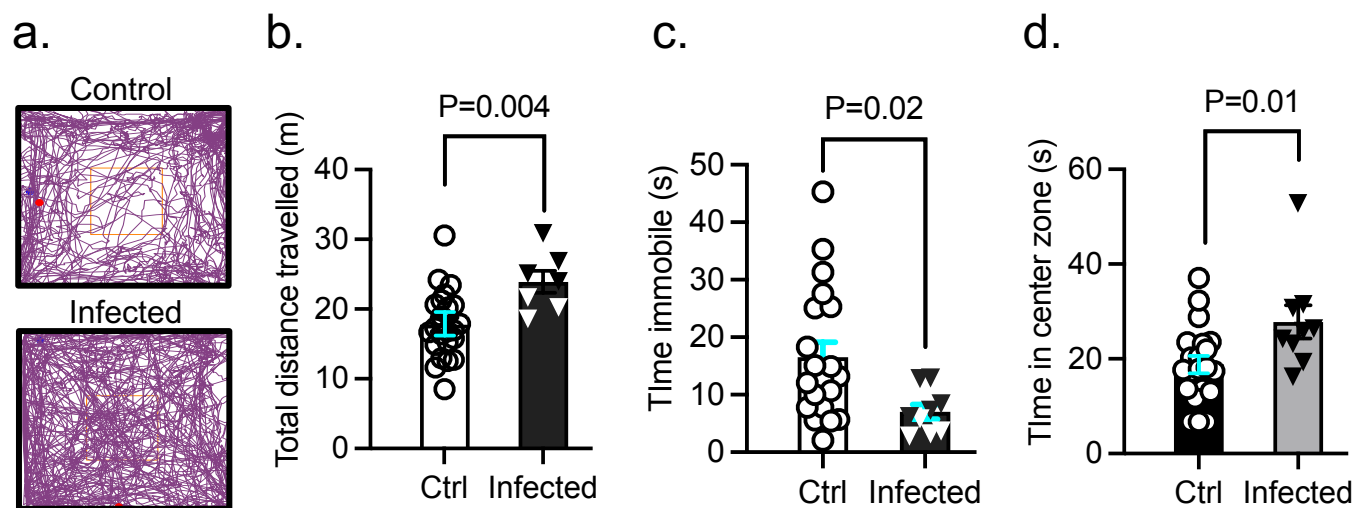**a.**

70-kDa

Ctrl

Infected

Signal intensity (more leakage)

b.

c.

d.

Ctrl H&E

Ctrl H&E

Infected H&E

Infected H&E

e.

Ctrl

Neutrophils
DAPI
Lectin

Infected

Neutrophils
DAPI
Lectin

Fig. 2.

a.

10-kDa

Ctrl

Infected

b.

P=0.03

c.

70-kDa

Ctrl

Infected

Signal intensity (more leakage) →

d.

P=0.01

e.

P=0.01

P=0.0002

f.

○ Control   ▼ Infected (7 d)
■ Infected (24 h)   ◆ Infected (1 m)

P=0.01

P=0.003

P=0.002

VE-cadherin   Occludin   Claudin-5

Fig. 3.

a.

Control

Infected

b.

P=0.004

c.

P=0.02

d.

P=0.01

Fig. 4.

a.

b.

Lung

c.

Spleen

d.

Cortex

e.

Choroid plexus

f.

Hippocampus

g.

Isolated capillaries

Ctrl

Infected

Cortex

Choroid plexus

Hippocampus

Isolated capillaries

Fig. 5.

a.

b.

○ Ctrl
● Infected

c.

d.

e.

Fig. 6.

Fig. 7.

a.

Legend:
- Vehicle (black)
- IL-1β (2 ng/mL) (pink)
- IL-1β (20 ng/mL) (blue)
- IL-1β (200 ng/mL) (green)
- IL-1β + TNFα (20 ng/nL) (orange)

Y-axis: Resistance Change (100, 75, 50, 25, 0, -25, -50, -75, -100)
X-axis: Time (hours) (0, 1, 2, 3, 4, 5, 6)

b.

Y-axis: % Decrease in TER (20, 0, -20, -40, -60, -80)
X-axis: Vehicle, 2, 20, 200 (IL-1β), IL-1β + TNFα
*P=0.001

c.

Vehicle — ZO-1 / Nuclei — 0 µm 25

IL-1β (20 ng/mL) — ZO-1 / Nuclei — 0 µm 25